



RESEARCH ARTICLE

The voltage-gated sodium channel pore exhibits conformational flexibility during slow inactivation

Soumili Chatterjee¹, Rajan Vyas¹ , Sreevatsa V. Chalamalasetti¹, Indra D. Sahu², Jérôme Clatot³, Xiaoping Wan³, Gary A. Lorigan², Isabelle Deschênes^{1,3}, and Sudha Chakrapani¹ 

Slow inactivation in voltage-gated sodium channels (Na_vs) directly regulates the excitability of neurons, cardiac myocytes, and skeletal muscles. Although Na_v slow inactivation appears to be conserved across phylogenies—from bacteria to humans—the structural basis for this mechanism remains unclear. Here, using site-directed labeling and EPR spectroscopic measurements of membrane-reconstituted prokaryotic Na_v homologues, we characterize the conformational dynamics of the selectivity filter region in the conductive and slow-inactivated states to determine the molecular events underlying Na_v gating. Our findings reveal profound conformational flexibility of the pore in the slow-inactivated state. We find that the P1 and P2 pore helices undergo opposing movements with respect to the pore axis. These movements result in changes in volume of both the central and intersubunit cavities, which form pathways for lipophilic drugs that modulate slow inactivation. Our findings therefore provide novel insight into the molecular basis for state-dependent effects of lipophilic drugs on channel function.

Introduction

Voltage-gated sodium channels (Na_vs) are an established molecular target in the treatment of neuropathic pain, cardiac arrhythmia, and epilepsy (Kaczorowski et al., 2008; Nardi et al., 2012; Catterall and Swanson, 2015). The therapeutic drugs currently in use to treat these conditions inhibit Na_v activity by blocking the channel pore and allosterically shifting the gating equilibrium toward the resting or inactivated state (Hille, 2001; Catterall, 2012). The Na_v open state is transient in nature and rapidly terminated by entry into inactivated states. In addition to the fairly well-understood mechanism of fast inactivation, which takes place within milliseconds and is believed to involve a physical pore block by a region between domains III and IV (Armstrong et al., 1973; Rojas and Rudy, 1976), Na_vs also exhibit inactivation on the slower timescales (seconds to minutes), the mechanisms for which are still unclear (Rudy, 1978). Slow inactivation reduces the availability of channels after a high-frequency stimulation or a prolonged depolarizing pulse, and manifests as hysteresis or “memory” of previous excitation (Narashashi, 1964; Toib et al., 1998). Consequently, slow inactivation regulates cellular excitability and controls neuronal properties such as firing rates and spike-frequency adaptation. The onset and recovery of slow inactivation varies over several orders of magnitude based on the frequency, amplitude, and duration of the activating pulses, and suggests that there may not be just one underlying mechanism,

but rather a complex interplay of multiple processes involving different regions of the channel (Narashashi, 1964; Toib et al., 1998; Ulbricht, 2005).

The structural basis for slow inactivation has remained elusive, partly because mutational hotspots that alter this process are distributed throughout the channel (Silva, 2014; Ahern et al., 2016). Based on the effects of toxins, permeant ions, and pore blockers, the selectivity filter (SF) region is implicated as the active center for slow inactivation, analogous to the C-type inactivation in K⁺ channels (Balser et al., 1996a; Townsend and Horn, 1997; Sandtner et al., 2004; Szendroedi et al., 2007; Capes et al., 2012). Mutations elsewhere in the protein, such as in the voltage-sensing domain (VSD), the S4-S5 linker, and the C-terminal end of S6, also dramatically alter slow inactivation (Ruben et al., 1992; Kontis and Goldin, 1997; Capes et al., 2012; Silva and Goldstein, 2013; Lenaus et al., 2017). Therefore, understanding the multifaceted cross-talk between different regions of the Na_v channel leading to slow inactivation has been a herculean task.

Prokaryotic Na_vs, with their overall structural, functional, and pharmacological conservation (Ren et al., 2001; Shaya et al., 2011; McCusker et al., 2012; Zhang et al., 2012; Sula et al., 2017), are still the most tractable system to investigate the mechanisms of gating and modulation. This is because the information regarding protein dynamics in native membranes

¹Department of Physiology and Biophysics, Case Western Reserve University, Cleveland, OH; ²Department of Chemistry and Biochemistry, Miami University, Oxford, OH; ³Heart and Vascular Research Center, Department of Medicine, Case Western Reserve University, Cleveland, OH.

Correspondence to Sudha Chakrapani: scx584@case.edu.

© 2018 Chatterjee et al. This article is distributed under the terms of an Attribution–Noncommercial–Share Alike–No Mirror Sites license for the first six months after the publication date (see <http://www.rupress.org/terms/>). After six months it is available under a Creative Commons License (Attribution–Noncommercial–Share Alike 4.0 International license, as described at <https://creativecommons.org/licenses/by-nc-sa/4.0/>).

can be directly combined with high-resolution structural data, and together these findings can be analyzed in the framework of detailed functional studies. Interestingly, although prokaryotic Na_vs lack fast inactivation, they appear to have preserved the hallmark features of slow inactivation (Pavlov et al., 2005; Lee et al., 2012; Payandeh et al., 2012; Zhang et al., 2012), and therefore, are ideal systems for probing the mechanism and regulation of this clinically critical Na_v phenomenon. Crystal structures of currently available Na_v reveal the VSD in its activated or “up” conformation and the pore domain (PD) in a closed conformation (either symmetrically, as seen in Na_vAb-217C [*Arcobacter butzleri*] structures, or asymmetrically, as in Na_vAb-WT and Na_vRh [*Rickettsiales* sp. HIMB114]; Payandeh et al., 2011, 2012; Zhang et al., 2012) or in an open conformation (as in Na_vMs [*Magnetococcus marinus*; Sula et al., 2017] and C-terminal truncated Na_vAb [Lenaues et al., 2017]). Additionally, the PD has been crystallized in either a closed (Na_vAe [*Alkalilimnicola ehrlichii*]) or an open (Na_vMs) conformation (Shaya et al., 2014; Naylor et al., 2016). The structures with a loss of fourfold symmetry (Na_vAb-WT and Na_vRh) are suggested to represent slow-inactivated states. However, to what extent these structures represent conformations on the membrane is still not resolved. Although the VSD conformation in these structures is as expected at 0 mV, the closed pore conformation is intriguing and in sharp contrast to the wide-open pores of all K_v structures (Jiang et al., 2003; Long et al., 2005, 2007). Although the loss of symmetry, as proposed, could be one potential mechanism of inactivation, conformational changes at the SF between the two Na_vAb structures (WT and 217C) are rather subtle and likely to be insufficient to impede permeation of partially hydrated sodium ions (Payandeh et al., 2012). The structural differences also do not account for the observed dramatic differences in pore blocker accessibilities or affinities in the closed and inactivated conformations (Hille, 1977; Ragsdale et al., 1994; Nau and Wang, 2004; Fozzard et al., 2005). This leads us to the following question: What are the conformational changes at the SF region associated with Na_v slow inactivation in a membrane environment?

A complete understanding of the conformational changes in the SF region during slow inactivation of Na_v in a physiological environment mandates a structural description of at least two conformational states: an activated-conductive state and a slow-inactivated conformation. Under steady-state conditions, at 0 mV membrane potential, the channels are expected to be predominantly in the slow-inactivated conformation. However, in Na_v channels, the open conductive conformation is transient and structurally not accessible under equilibrium conditions. To circumvent this problem, we use the isolated PD as a surrogate for the conductive conformation. The isolated PD opens stochastically and is less prone to slow inactivation, in the absence of the voltage-sensor domain. By using site-directed spin labeling and EPR spectroscopy, we map out differences in the spin label dynamics and solvent accessibility at equivalent positions in the two channel constructs. The extent of these changes is quantified by double electron-electron resonance spectroscopy (DEER) distance measurements to elucidate the conformational changes underlying slow inactivation.

Materials and methods

Cloning and protein expression

The full-length (Na_vSp1) and the PD construct (residues F122-K258, Na_vSp1-P) of voltage-gated sodium channel from *Silicibacter pomeroyi* in modified pET24b vector were a gift from Daniel Minor, Jr. (University of California, San Francisco, San Francisco, CA). Na_vSp1-pET24b construct carries an N-terminal His₈-tag and HRV-3C protease cleavage site. Na_vSp1-P-pET24b construct carries an N-terminal His₆-tag, maltose-binding protein, and HRV-3C protease cleavage site. Both proteins were expressed and purified using previously published protocols with modifications (Shaya et al., 2011). In brief, C43 (BL21 (DE3)) *Escherichia coli* cells (Lucigen) transformed with the constructs were grown in 1L of Terrific Broth media containing 50 µg/ml kanamycin (Gibco) at 37°C to OD₆₀₀ of 0.4. Afterward, the temperature was reduced to 18°C and the cells were grown until the OD₆₀₀ reached 1.0. The cells were then induced with 0.4 mM isopropyl 1-thio-β-D-galactopyranoside (GoldBio) overnight at 18°C. Membranes were prepared by homogenizing the cells in Buffer A (300 mM NaCl, 20 mM Tris-HCl, pH 8.0) with protease inhibitors (Roche), and centrifuged at 167,000 ×g for 45 min. Unbroken cells and debris were separated by centrifugation (14,000 ×g at 4°C, 15 min) and the supernatant was then ultracentrifuged (167,000 ×g at 4°C, 45 min) to pellet and separate the membranes from the supernatant. Na_vSp1 and Na_vSp1-P membranes were solubilized in Buffer B (200 mM NaCl, 20 mM Tris base, 8% vol/vol glycerol, pH 8.0) supplemented with either 40 mM *n*-dodecyl-β-D-maltopyranoside (DDM; Anatrace) or 40 mM *n*-decyl-β-D-maltopyranoside (DM; Anatrace), respectively, at 4°C. Na_vSp1 was purified by binding to Ni-NTA (Ni²⁺ loaded on to agarose-derivatized nitriloacetic acid chelation moiety) resin (Qiagen; equilibrated with Buffer B in 1 mM DDM) for 2 h, washed with Buffer B containing 20 mM imidazole (Sigma-Aldrich), 0.5 mM tris(2-carboxyethyl)phosphine (TCEP; Amresco), and 1 mM DDM, pH 7.4, and eluted with Buffer B containing 300 mM imidazole, 1 mM DDM, and 0.05 mM TCEP, pH 7.4. Na_vSp1-P was purified by binding to amylose resin (New England BioLabs), washed with Buffer B containing 0.5 mM TCEP and 2.7 mM DM, pH 7.4, and eluted with Buffer B containing 40 mM maltose, 2.7 mM DM, and 0.05 mM TCEP, pH 7.4. The maltose-binding protein tag was cleaved with HRV-3C protease for 4 h at 4°C.

Site-directed spin labeling

One native cysteine in Na_vSp1 at position 51 (in the VSD) was mutated to serine and used as the template to generate mutants of interest. Removal of the VSD to generate the Na_vSp1-P construct leads to a cysteine-less template. Mutant proteins were expressed similar to the WT constructs. The affinity purified protein was labeled with a methanethiosulfonate spin probe (1-oxyl-2,2,5,5-tetramethylpyrrolidin-3-yl) methyl methanethiosulfonate (MTSL; Toronto Research) at a 10:1 label/protein molar ratio and incubated on ice for 1 h, after which a second dose of MTSL was added in a 5:1 molar ratio and further incubated on ice for 1–5 h. The labeled protein was purified by size exclusion chromatography on a Superdex 20/200 column (GE Healthcare). Spin-labeled samples were reconstituted at

a 1:3,000 protein:lipid molar ratio in a mixture of asolectin or dioleoyl-3-trimethylammonium-propane (DOTAP; Avanti Polar Lipids) lipid, incubated with biobeads (80 mg) overnight at 4°C, and centrifuged ($167,000 \times g$ at 4°C, 2 h) to obtain a pellet of the proteoliposomes.

EPR spectroscopy and analysis

Continuous wave (CW)-EPR spectroscopy (CW-EPR) measurements were performed at room temperature on a Bruker EMX X-band spectrometer equipped with a dielectric resonator and a gas-permeable TPX plastic capillary. First derivative absorption spectra were recorded at an incident microwave power of 2.0 mW, modulation frequency of 100 kHz, and modulation amplitude of 1.0 G. Our analyses were centered on two types of dynamic EPR structural information (Farahbakhsh et al., 1992; Altenbach et al., 2005). The first is the mobility of the spin probe, calculated as the inverse of the central line width of the first derivative absorption spectra (ΔH_0^{-1}). This parameter is governed both by the local steric contacts in the immediate vicinity of the probe and by the flexibility of the backbone to which it is attached (Mchaourab et al., 1996). As the frequency of nitroxide rotational motion is reduced, as witnessed in the presence of tertiary or quaternary contacts, the ΔH_0^{-1} value decreases for any particular motional geometry. On the contrary, structural motions leading to an increase in the probe's freedom of movement is reflected as an increase in ΔH_0^{-1} . The second is spin probe solvent accessibility evaluated by collisional relaxation methods. Here, nonpolar molecular oxygen (O_2) serves as a contrast agent to evaluate membrane accessibility, whereas polar Ni(II) ethylenediaminediacetic acid (NIEDDA) reports the extent of aqueous exposure (Farahbakhsh et al., 1992; Gross and Hubbell, 2002). The accessibility parameter (Π) is estimated from power saturation experiments in which the vertical peak-to-peak amplitude of the central line of the first derivative EPR spectra is measured as a function of increasing incident microwave power (Farahbakhsh et al., 1992).

DEER measurements

Intersubunit distances ($<50 \text{ \AA}$) were measured using DEER methods (Jeschke et al., 2002; Zou and Mchaourab, 2010) for spin-labeled samples in detergents. The spin labeling efficiency was determined as the ratio of the molar concentration of spin label determined by CW-EPR spectra and the protein concentration determined at UV (280) absorbance using a nanodrop spectrometer. The protein concentration range included $\sim 250 \mu\text{M}$, and the spin labeling efficiency ranged between 50–75% based on the position tested. Four-pulse DEER experiments were performed using a Bruker ELEXSYS E580 spectrometer equipped with a SuperQ-FT pulse Q-band system with a 10-W amplifier and EN5107D2 resonator. The sample was loaded into a 1.1-mm inner diameter quartz capillary (Wilma LabGlass) and mounted into the sample holder (plastic rod) inserted into the resonator. Dipolar time evolution data were obtained at 80 K using a standard DEER four-pulse sequence $(\pi/2)\text{mw1}-\tau_1-(\pi)\text{mw1}-\tau_1-(\pi)\text{mw2}-\tau_2-(\pi)\text{mw1}-\tau_2\text{-echo}$ (Pannier et al., 2000) at Q-band frequency ($\sim 33.9 \text{ GHz}$). The experimental conditions included pulse lengths of 10 and 20 ns for $(\pi/2)\text{mw1}$ and $(\pi)\text{mw1}$, respec-

tively; 24 ns for $(\pi)\text{mw2}$, 80 MHz of frequency difference between probe and pump pulse, shot repetition time determined by spin-lattice relaxation rate (T_1), 100 echo/point, and 2-step phase cycling. Data were collected out to $\sim 2.0 \mu\text{s}$ for overnight data acquisition time. DEER signals were background corrected assuming a 3-D homogeneous background and analyzed by the Tikhonov regularization in the DEER Analysis 2014 software (Chiang et al., 2005; Jeschke et al., 2006) to determine average distances and distributions in distance. The regularization parameter in the L curve was optimized by examining the fit of the time domain. The background factor takes into consideration contributions from intermolecular spin interaction leading to signal decay. Determination of the correct background subtraction is nontrivial and incomplete background correction could result in distance peak artifacts (Polyhach et al., 2007). This limitation is further confounded in liposome samples because of shorter dipolar evolution times, lower sensitivity, and higher background contribution through intermolecular interactions. Therefore, DEER data were collected in detergent samples, and for each dataset, different backgrounds were tested by moving the starting point of the background fit to identify the best fit. Previous studies confirm that there are no significant conformational differences in the detergent environment (Bagn  ris et al., 2014; Arrigoni et al., 2016).

To ensure that the distance peaks are real interspin distances and not ghost peaks arising as an artifact of the presence of multiple dipolar coupled spin labels in a symmetrical system, we performed suppression of ghost distances using power scaling of the form factor (primary DEER data/background function) with an exponent $\xi_N = 1/(1-N)$ with $n = 4$ (for four-spin system) in the DEER Analysis software (von Hagens et al., 2013; Fig. S3). The orientation dependence of DEER was assessed by measuring the effect of pump/probe position on the distance distribution for representative positions (Figs. S4, S5, and S6).

Electrophysiology

$\text{Na}_v\text{Sp1}$ was cloned into the pIRES2-EGFP vector, and all the $\text{Na}_v\text{Sp1}$ mutants were made using the QuickChange Site-Directed Mutagenesis kit (Stratagene) and sequenced before recordings. Human embryonic kidney cells (HEK-293) were grown at 37°C under 5% CO_2 , in Dulbecco's modified Eagle's medium supplemented with 10% FBS, 10% L-glutamine, and antibiotics (100 IU ml^{-1} penicillin and 100 mg ml^{-1} streptomycin). HEK-293 cells were transfected (in 35-mm-diameter wells) with PolyFect (Qiagen). Transfected cells were identified visually under the UV microscope by enhanced GFP expression. A whole-cell patch clamp was used to record Na^+ current at room temperature ($23 \pm 2^\circ\text{C}$) 24 h post-transfection. Acquisition and analysis were performed using an Axopatch 200B amplifier, digitized at 10 kHz sampling frequency, and analyzed using Clampfit 10.2. Pipettes were pulled from borosilicate glass capillaries to obtain 2.5 M Ω resistances. Pipette solution contained the following, in mM: 120, Cs methanesulfonate; 8, NaCl; 10, EGTA; 2, Mg-ATP; and 20, HEPES (pH 7.4 with CsOH). Bath solution contained the following, in mM: 155, NaCl; 1, CaCl_2 ; 1, MgCl_2 ; 5, KCl; 10, HEPES; and 10, glucose (pH 7.4 with NaOH).

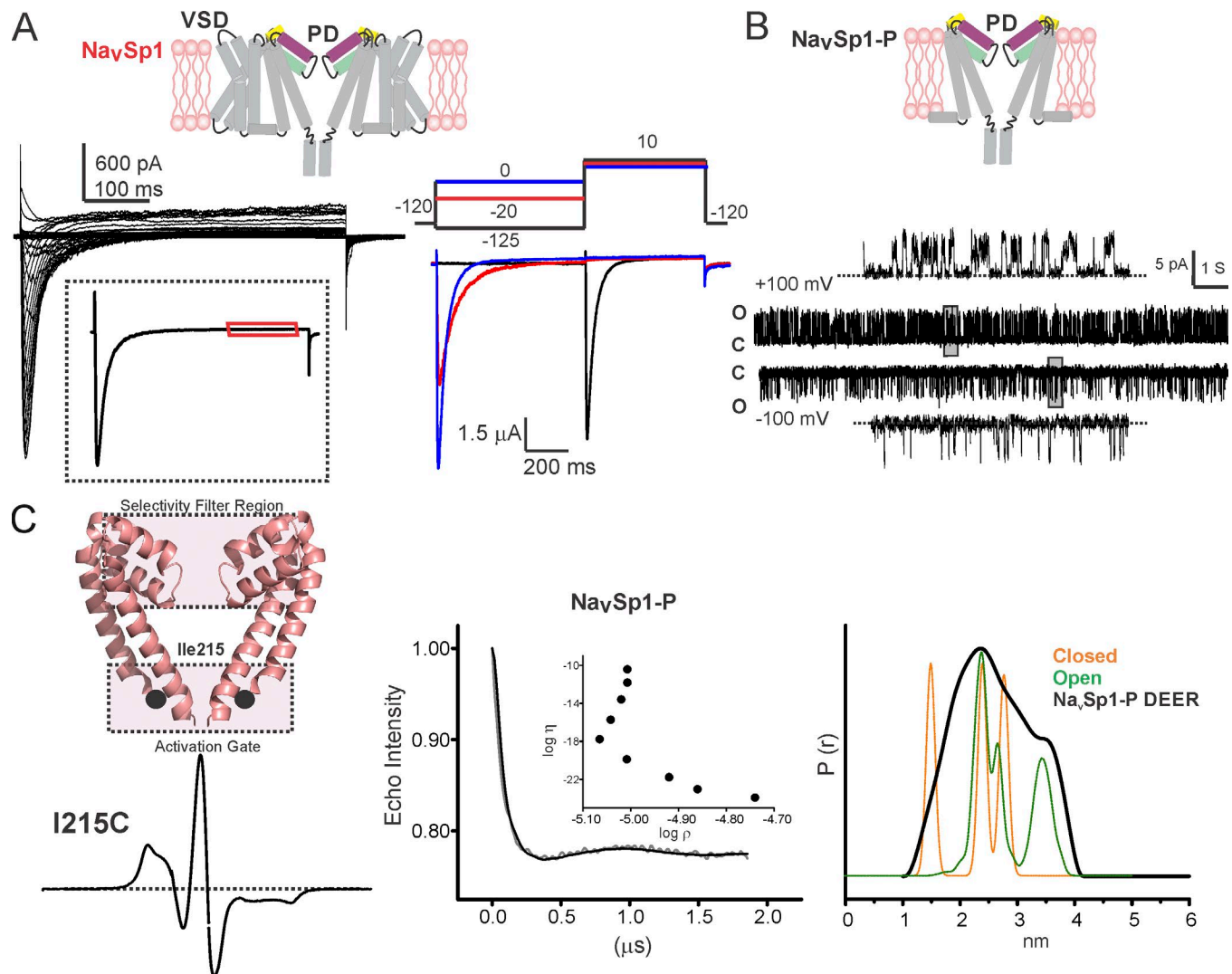


Figure 1. NavSp1-P pore-domain adopts a conductive conformation. (A) A schematic representation of the full-length NavSp1 with the VSD and the PD marked. Only two subunits are shown for clarity. An exemplar recording of NavSp1 whole-cell Na^+ currents. The activation protocol consisted of 500-ms depolarization from -80 to $+40$ mV in 5-mV increments from a holding potential of -120 mV with a sweep-to-sweep interval of 4 s. The inset shows a typical response to 0-mV depolarization pulse, where the steady-state open probability is less than 5% of the peak value (left). NavSp1 currents elicited by pulse-protocol (shown above). At the end of a 0-mV prepulse, the test pulse to 10 mV evokes minimal inward current, indicating that the channels are inactivated at the end of the prepulse (right). (B) Single-channel recordings of NavSp1-P reconstituted in liposomes (a schematic of NavSp1-P shown above) show functionally active channels that stochastically open and close. The trace within the gray box is shown in an expanded scale. C and O denote the closed and open states. The dotted line marks the zero-current level. (C) Two diagonal subunits of closed-gate NavAb crystal structure (PDB ID 3RVY) with the position at the bundle crossing (I215) shown as black spheres. The boxed regions highlight the activation gate and the selectivity filter region in the channel. Spin-normalized CW-EPR spectra of NavSp1-P I215C in asolectin membrane (bottom). Background-corrected Q-band DEER echo intensity is plotted against evolution time for I215R1 in DM (middle panel) and fit using model-free Tikhonov regularization. The Tikhonov L-curve is shown in the inset. The corresponding interspin distance distribution with regularization parameter ($\alpha = 100$) is shown in the right panel, with two distributions corresponding to the distances between the adjacent and nonadjacent subunits. For the position I215C, interspin distance distributions were simulated with Nav structures (PDB ID 3RVY for closed, orange; and PDB ID 3ZJZ for open, green) based on analysis of spin label rotamers using the MMM software package (Polyhach et al., 2007, 2011). Rotamer library calculations were conducted at 83 K.

Electrophysiology in reconstituted liposomes

Electrophysiological measurements were made by patch-clamp recordings in channel-reconstituted liposomes prepared as described earlier (Delcour et al., 1989; Cortes et al., 2001; Chakrapani et al., 2007; Velisetty and Chakrapani, 2012). Purified NavSp1-P from size exclusion chromatography was reconstituted into preformed asolectin vesicles (channels were reconstituted in 1:10,000 protein/lipid) by diluting in 150 mM NaCl and 10 mM MOPS, pH 7.0 (reconstitution buffer). Detergent was removed

by incubating the proteoliposome suspension with biobeads (Bio-Rad) overnight at 4°C . The suspension was centrifuged at $100,000 \times g$ for 1 h and the pellet resuspended in reconstitution buffer. A drop of the proteoliposome was placed on a glass slide and dried overnight in a desiccator at 4°C . The sample was then rehydrated with 20 μl of buffer, which yielded giant liposomes. All current measurements were made at room temperature by inside-out patch clamping of proteoliposome under symmetrical NaCl concentrations. Recording pipettes were pulled from thin-

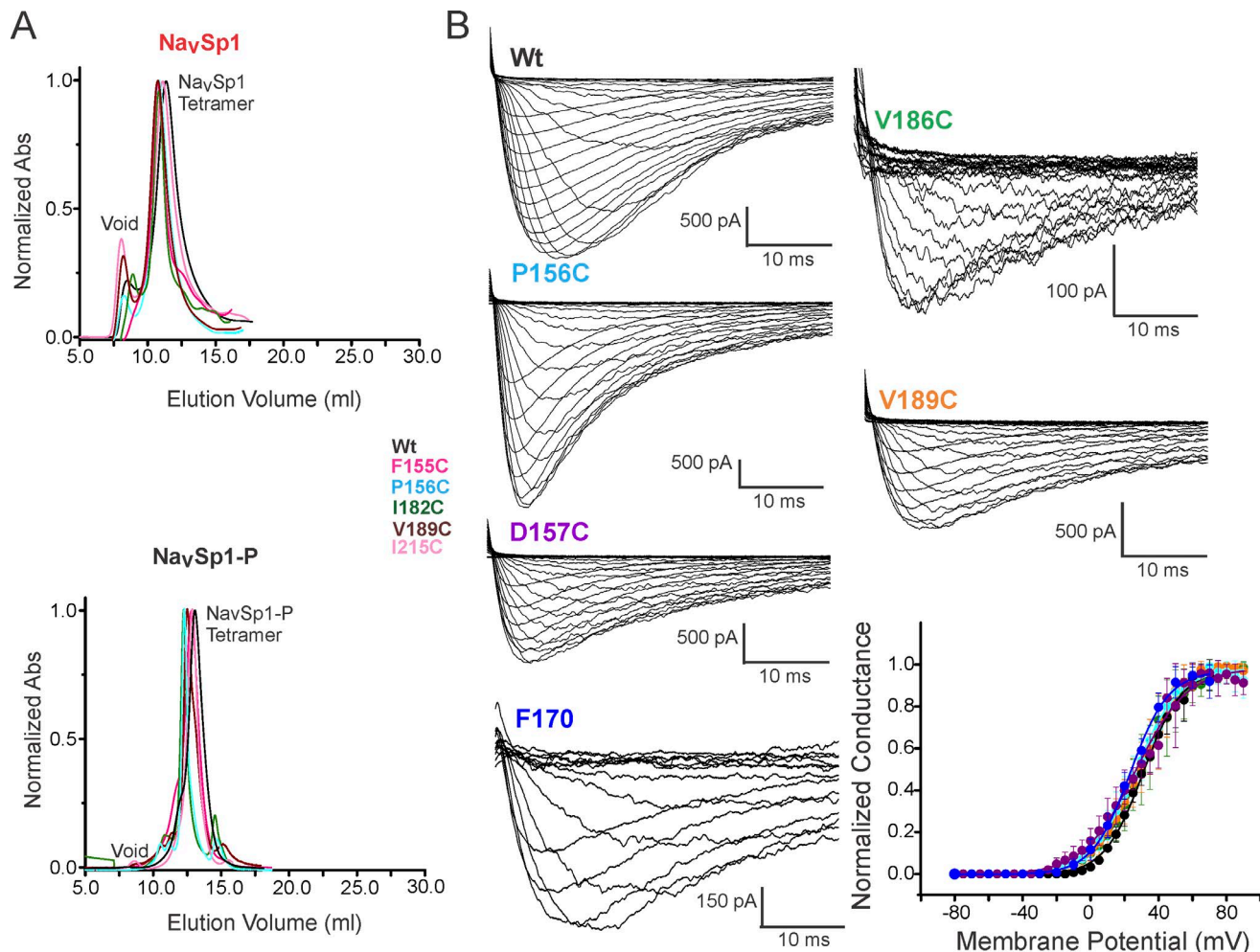


Figure 2. Characterization of individual cysteine mutants. (A) Elution profiles from size exclusion chromatography for WT and representative spin-labeled cysteine mutants before reconstitution. (B) Whole-cell current traces for representative NavSp1 cysteine mutants recorded from HEK-293 cells in response to an activation protocol consisting of 500-ms depolarizations from -80 to $+100$ mV in 5 -mV increments from a holding potential of -120 mV with a sweep-to-sweep interval of 4 s. The bottom panel is the voltage dependence of activation for WT and cysteine mutants. The $V_{1/2}$ of activation is WT (28.9 ± 0.5 mV, $n = 3$); P156C (26.1 ± 0.5 mV, $n = 3$); D157C (25.5 ± 0.7 mV, $n = 3$); F170C (21.2 ± 1.1 mV, $n = 4$); V186C (29.0 ± 0.4 mV, $n = 4$); and V189C (29.0 ± 0.4 mV, $n = 3$). The vertical lines show SD from “ n ” individual measurements.

walled borosilicate glass, heat-polished to a resistance of 1.5 – 2 M Ω , and filled with 150 mM NaCl and 10 mM MOPS, pH 7.0 . Currents were measured using Axopatch 200B, digitized at 10 kHz sampling frequency, and analyzed using Clampfit 10.2.

Online supplemental material

Figs. S1 through S6 present primarily methods and validation of the results obtained by CW-EPR and DEER spectroscopy.

Results

Slow inactivation is reduced in the isolated PD construct

The prokaryotic Nav homologue from *S. pomeroyi* (NavSp1) expressed in HEK-293 cells displays voltage-activated currents with a $V_{1/2}$ value of 28.9 ± 0.5 mV (Fig. 1A, left). The voltage-activated gating is right shifted in comparison to other bacterial Nav homologues (particularly in comparison with NavAb, which has a $V_{1/2}$ of -98 mV; Payandeh et al., 2011; Arrigoni et al., 2016; also see Fig. 2B). In response to a test pulse of 0 mV, the channels

are seen to activate and then inactivate within seconds, such that very little currents are seen at steady-state (highlighted by the red box in Fig. 1A; a representative current trace shown in the inset). A second depolarizing pulse to $+10$ mV at the end of the 0 mV pulse shows minimal current confirming that channel activity was lost because of inactivation (Fig. 1A, right). In contrast, reconstituted isolated PD construct (referred to as NavSp1-P) shows robust steady-state currents (Fig. 1B) with open probability as high as ~ 0.7 (Shaya et al., 2011). This suggests that in the absence of the VSD, the isolated PD can open and close stochastically with negligible voltage dependence. To determine the extent of opening at the S6-activation gate, we performed site-directed spin labeling at a residue close to the S6 bundle-crossing (I215C) and measured the spectra by CW-EPR spectroscopy in reconstituted liposomes. The S6 bundle crossing is implicated to undergo widening as the channel opens (Sula et al., 2017), leading to differential solvent accessibilities in the closed and open states (Oelstrom and Chanda, 2016). If the S6 helices in NavSp1-P are closed as in the NavAb structure, the near proximity of the spin

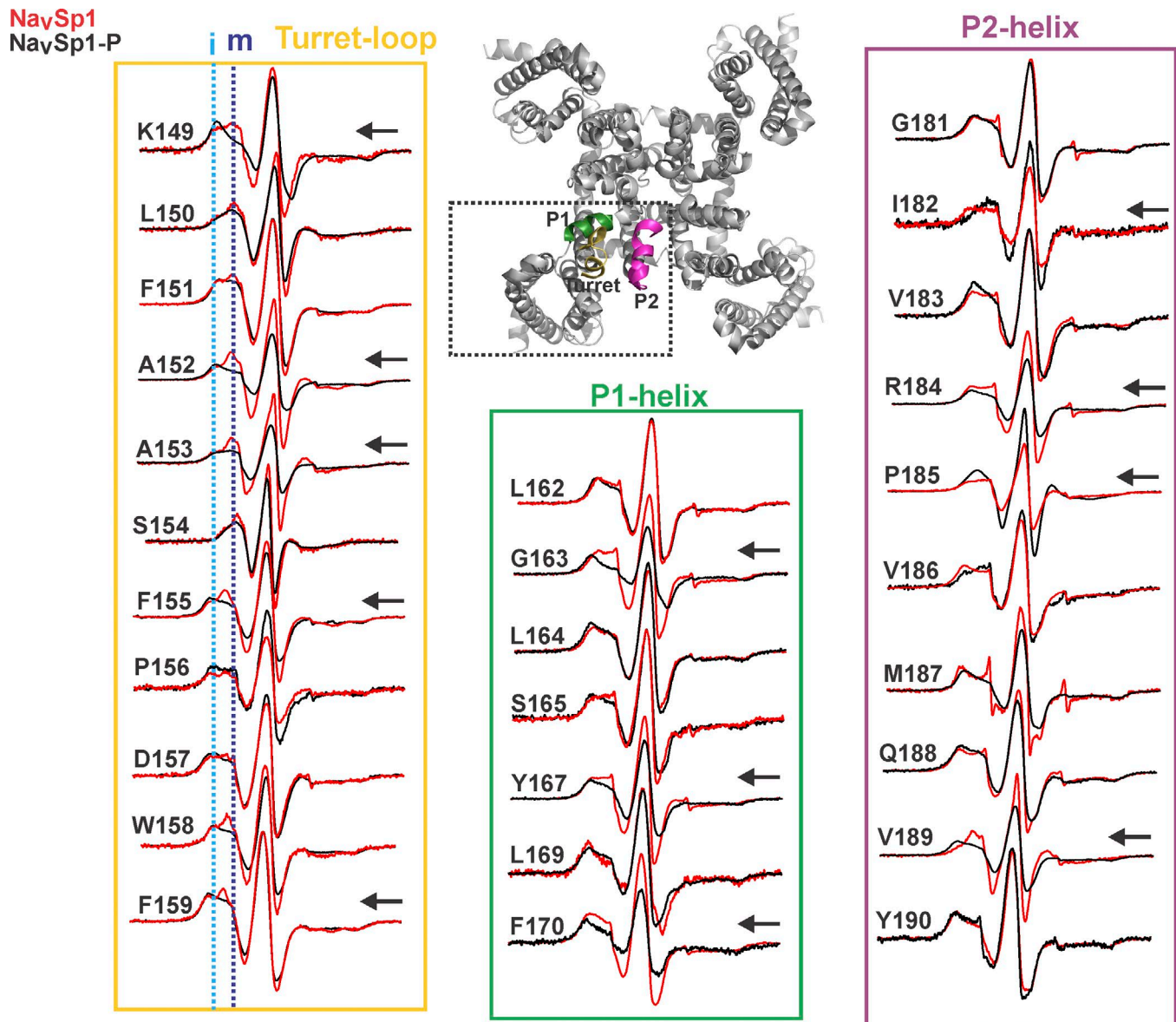


Figure 3. **Conformational differences in the selectivity filter region of NavSp1 and NavSp1-P.** Spin-normalized CW-EPR spectra for positions along the turret loop, P1 helix, and P2 helix in NavSp1 (red) and NavSp1-P (black). These regions are color-coded on the NavAb structure (PDB ID 3RVY). Dotted lines marked as “i” and “m” represent the immobile and mobile components of the spectra, respectively. The two components may arise from two different rotameric orientations of the spin labels and/or from two conformational states of the protein in equilibrium. Arrows highlight positions with the most prominent differences in line shapes in the two channels.

labels (under 7 Å) will lead to dipolar broadening of the spectra. In contrast, we found minimal dipolar coupling at this position, suggesting that the helices are likely splayed open (Fig. 1C, left). We then measured interspin distances at I215C between subunits using DEER. The resulting distance distribution profile is broad and reveals peaks at ~22 and ~32 Å for adjacent and diagonal intersubunit distances, respectively. These distances are longer than the expected distances for the closed channel (the cβ-cβ distances for adjacent and diagonal subunits are 7 and 14 Å in the closed NavAb structure and are 18 and 26 Å in the open NavMs-P structure; Payandeh et al., 2011; Naylor et al., 2016; Fig. 1C, right). The experimental distance distribution was then compared with simulated DEER distances at the I215 position in the closed NavAb and open NavMs-P channels calculated using the Mul-

tiscale Modeling of Macromolecular systems (MMM) software package (Polyhach et al., 2007, 2011; Fig. 1C). The overlay shows that the measured distribution aligns better with the distances calculated from the open NavMs-P (green line) than the closed NavAb (brown line), thereby revealing that the S6 in NavSp1-P is predominantly in the open conformation. Both electrophysiological studies and EPR data lend support to the idea that NavSp1 and NavSp1-P are likely to be models for the slow-inactivated channel and the conductive pore, respectively.

Conformational differences between NavSp1 and NavSp1-P in a membrane environment

To probe the conformation of the pore in NavSp1 and NavSp1-P, we used site-directed spin labeling/CW-EPR methods in mem-

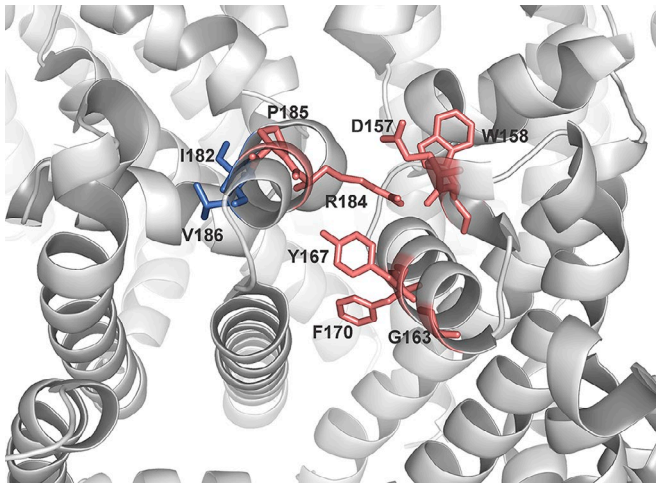


Figure 4. A close-up view of the intersubunit cavity in the NavAb structure. Residues that show a prominent increase in mobility in NavSp1 in comparison to NavSp1-P are shown in red, and those that show a decrease in this parameter are represented in blue. The residues with higher mobility values are found to line the intersubunit cavity, which is at the interface of P1 and P2 helices from two adjacent subunits.

brane-reconstituted channels. Structural differences were characterized by a systematic evaluation of the probe dynamics and solvent accessibility (lipid versus water) of the pore region. CW-EPR spectral analysis included the determination of two parameters: (1) motional freedom of the nitroxide spin probe (ΔH_0^{-1}), which is measured as the inverse of the central line width of the first derivative absorption spectra; this line shape parameter is used to assess changes in mobility, and thus about the changes in the local environment; and (2) solvent accessibility (Π) to either membrane or water measured by collisional relaxation in the presence of lipid-soluble oxygen (O_2) and water-soluble IINiEDDA, respectively.

Single-cysteine mutations in the outer pore region (the turret loop, P1 and P2 helices) were generated on a cys-less background (C51S). The residues comprising the SF (Gln171-Met180) were left unperturbed. The individual cysteine mutants were expressed in *E. coli*, purified, labeled with MTSL (Fig. 2 A), and reconstituted in asolectin membranes using previously established methods (McCusker et al., 2012; Velisetty et al., 2012). Because there is no simple cellular assay to rapidly check the functionality of each mutant, we chose representative cysteine mutants to assay the functionality by whole-cell patch clamp recordings in transiently transfected HEK-293 cells (Fig. 2 B). An overlay of the EPR line shapes for all of the positions studied in NavSp1 and NavSp1-P are shown in Fig. 3. A visual examination of the spectra shows prominent differences in line shapes in the two channels at several positions in the turret loop, P1 and P2 helices (marked by black arrows). This is in sharp contrast to minimal changes observed in these regions in the crystal structures (Payandeh et al., 2011, 2012; Sula et al., 2017). In general, NavSp1 spectra at these positions were more mobile in comparison to NavSp1-P, suggesting that the SF region is more dynamic in NavSp1. Notably, the spectra for most positions in the turret loop (Lys149-Phe159) of NavSp1 revealed two distinct components: an immobile component that essentially overlaps with the NavSp1-P spectra (indicated by the

light blue line) and an additional mobile component (indicated by the dark blue line). The two spectral components in the EPR signal could arise from two different scenarios. In one, there is an equilibrium between two distinct channel populations, and in each population, the spin label has a different environment. In the second, there are two spin-rotameric orientations for the channel in a given conformation, and these rotamers have distinct environments. Residues Gly163, Tyr167, and Phe170 in the P1 helix and residues Arg184 and Pro185 in the P2 helix show the most prominent increase in mobility in NavSp1 (black arrows in Fig. 3). Interestingly, these residues line an intersubunit cavity interfaced by P1 and P2 helices from adjacent subunits (Fig. 4). On the other hand, residues that show a decrease in mobility, particularly Ile182 and Val186, lie on the opposite face of the P2 helix away from the intersubunit cavity. These findings highlight the conformational differences in the SF region in membrane-reconstituted NavSp1 and NavSp1-P channels.

A complete plot of probe mobility (ΔH_0^{-1}) and accessibility parameters is presented for NavSp1 and NavSp1-P (Fig. 5 A; see Materials and methods for details on the estimation of these parameters). Within each dataset, as expected, the turret loop and the P2 helix residues are highly mobile (top panel), and several positions have substantial water exposure (bottom panel). The probe mobility clearly tracks the α -helical periodicity in the N-terminal end of the turret loop (residues 149–155) and the P2 helix. The membrane boundaries are delineated by a drop in aqueous exposure at Phe154 and Val190 in the turret loop and P2 helix, respectively. The buried environment of P1 is evident in its overall lower mobility and water/lipid accessibility. However, the most remarkable finding is that there are notable differences in the probe mobility and accessibility parameters between NavSp1 and NavSp1-P channels at several positions. In addition to an overall increase in dynamics, the equivalent positions in NavSp1 showed higher accessibility to lipids than NavSp1-P (marked by blue circles). When the differences in values of Π_{O_2} parameters between the two channels were mapped on the NavAb structure, residues with higher lipid accessibility in NavSp1 were found to line the intersubunit cavity (Fig. 5 B). This also matches the pocket of increased side-chain dynamics (Fig. 4). A plot of the average lipid accessibility as a function of the mobility parameter (Fig. 5 C) reveals that the SF region is more dynamic and lipid-exposed in NavSp1. This increase is most pronounced in the turret loop and followed by the P1 helix and then the P2 helix (Fig. 5 C; the length and the slope of the dotted lines). Based on these findings, we suggest that the SF region is substantially different in the conformation adopted by NavSp1 and NavSp1-P.

Extent of conformational changes in the selectivity filter region

What is the conformational change that brings about the observed differences in mobility and lipid accessibility in the SF region? To quantify the magnitude of conformational differences between NavSp1 and NavSp1-P SF regions, we determined average interspin distances between the subunits in the two channels by Q-band DEER (see Materials and methods, Fig. S1). Because DEER measurements are complicated in liposome samples due to shorter dipolar evolution times, lower sensitivity, and higher

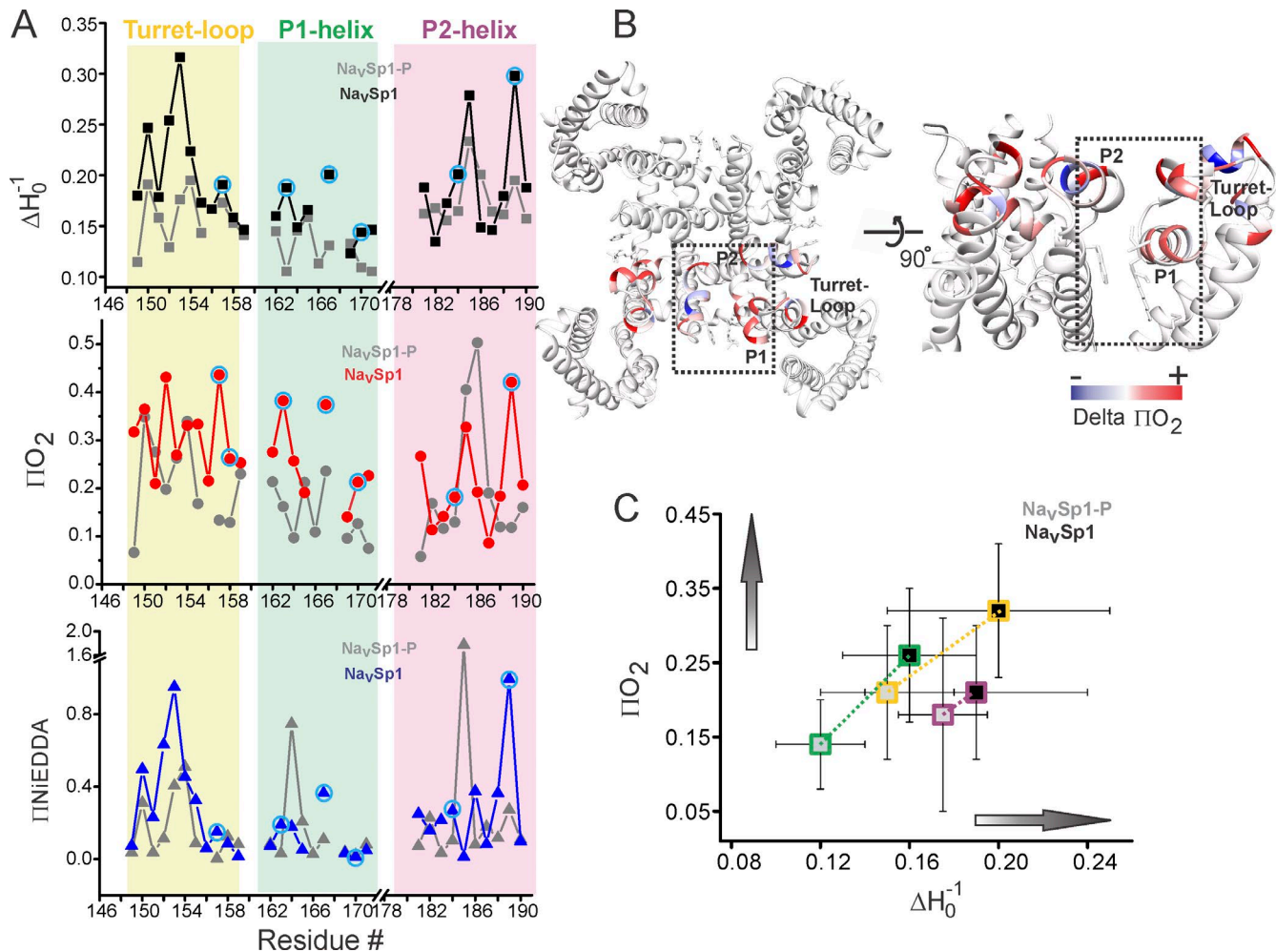


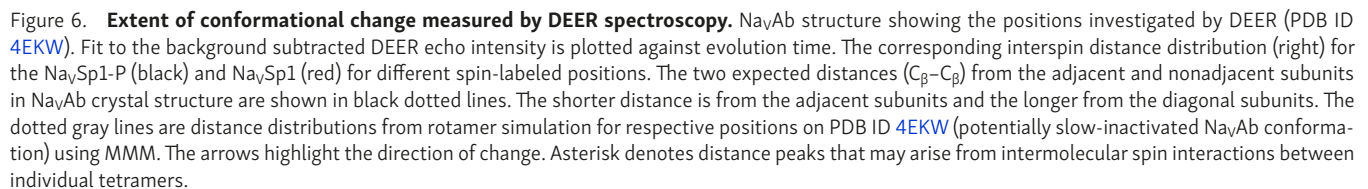
Figure 5. EPR environmental parameters reveal conformational differences in the membrane-embedded NavSp1 and NavSp1-P. (A) A plot of residue environmental parameters for NavSp1-P (shown in gray) and NavSp1 (shown in color). ΔH_0^{-1} parameter (top); O_2 accessibility, ΠO_2 (middle); water accessibility, $\Pi NIEDDA$ (bottom). The EPR parameters for continuous positions are linked by solid lines. Residues that were not studied (because of sub-optimal expression/oligomeric stability) appear as gaps. Positions revealing prominent changes are highlighted within blue circles. (B) Difference in ΠO_2 values between the NavSp1 and NavSp1-P are mapped on the NavAb structure (PDB ID 3RVY) and color-coded, red denoting an increase and blue representing a decrease in the environmental parameter. (C) A plot of the average lipid accessibility (ΠO_2) as a function of the average mobility parameter ΔH_0^{-1} for the turret loop (yellow), P1 helix (green), and P2 helix (magenta). The light gray boxes represent NavSp1-P, and the black boxes denote NavSp1. The dotted lines connecting the light and black boxes for each region signify the magnitude of difference between the EPR environmental parameters in the two channels.

background contribution, these measurements were collected in detergent samples. In each case, as expected for a symmetric tetrameric system, the distance distribution shows at least two main components, one corresponding to the short adjacent distance and the other to the long nonadjacent distance (Fig. 6). For positions Ala153, Phe155, and Pro156 in the turret loop, the DEER distances in NavSp1-P are consistent with the Nav crystal structures (C β -C β distances calculated in NavAb, PDB ID 3RVY, indicated by black dotted lines, Fig. 6). A comparison of the distance distribution for these positions in NavSp1 revealed an interesting trend of protein motion. Although the distance peaks for A153 were identical and essentially overlapped in both channels, the distance distribution for positions Phe155 and Pro156 in NavSp1 were broader and progressively moved toward longer distances when compared with NavSp1-P. Interestingly, simulated distance distribution calculated using MMM software (Polyhach et al., 2007, 2011) on the “potentially inactivated” NavAb structure (PDB ID 4EKW) also shows

multiple peaks at several positions, arising from the loss of four-fold symmetry (gray dotted lines, Fig. 6). Differences in distance distribution between NavSp1 and NavSp1-P were also observed for positions along P1 and P2 helices, albeit in the opposite direction. In comparison to NavSp1-P, for Tyr167 and Phe170 in the P1 helix, the NavSp1 distance peaks had additional components that appeared at shorter distances. On the other hand, for positions along P2 helix, namely Val183, Arg184, Val186, Val189, and Trp194, the DEER distributions consistently had longer components in NavSp1. These results point to a rearrangement of the P1 and P2 helices with respect to each other, such that P1 helix moves closer to the pore axis, whereas P2 helix moves away from it.

Conformation of the SF region with the VSD in its “down” conformation

To further assess if the observed conformational differences in SF region in NavSp1 and NavSp1-P indeed reflect structural changes



To test if the SF region conformation in Na_vSp1 resting state is similar to that of Na_vSp1-P, we reconstituted representative spin-labeled Na_vSp1 mutants in the P2 helix in DOTAP lipids. The measured CW-EPR spectra under these conditions were compared with Na_vSp1 and Na_vSp1-P spectra in aolectin. In aolectin, positions Ile182 and Val186 are more immobile in Na_vSp1 than in Na_vSp1-P (Fig. 7, left panel). In DOTAP, these positions become more mobile (Fig. 7, right panel) such that they now closely resemble Na_vSp1-P spectra (Fig. 7, middle panel, gray box). In contrast, Val189 is more mobile in Na_vSp1 compared with Na_vSp1-P, but in DOTAP, its mobility decreases with the appearance of the immobile component. To verify that the observed effects on spectral line shapes in Na_vSp1 reconstituted in DOTAP arose from conformational changes induced by the VSD, we measured the spectra of DOTAP-reconstituted Ile182 and Val186 mutants

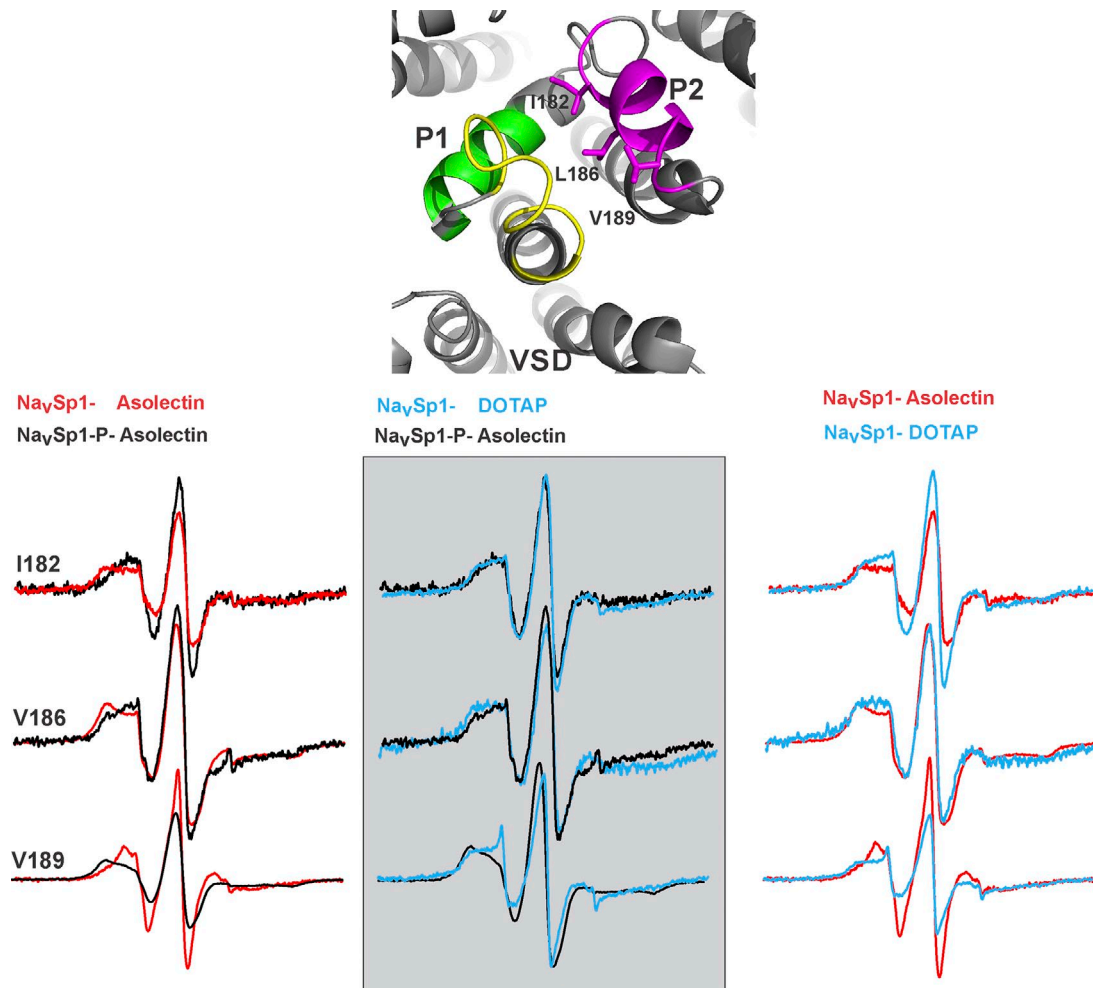


Figure 7. **Spectral changes at the SF region underlying transitions between the putative resting/conductive and slow-inactivated states.** CW spectra for NaVSp1 at representative positions in the P2 helix (positions marked on the NaVAb structure) reconstituted in asolectin (red) and DOTAP (cyan) and compared with NaVSp1-P reconstituted in asolectin (black). A similarity of NaVSp1-DOTAP and NaVSp1-P-asolectin spectra is highlighted in the gray box.

on the NaVSp1-P template (Fig. S2). As expected, there were no differences in the line shapes from asolectin and DOTAP samples, confirming that DOTAP had no effect on the dynamics of the PD. Therefore, the pore conformation in NaVSp1 is sensitive to the membrane lipid environment and capable of switching between resting and inactivated conformational states.

Functional validation of the proposed model

The CW and pulsed EPR data reveal conformational differences in the pore region of NaVSp1-P and NaVSp1, which suggests that the two channels adopt distinct functional states. Functional studies show that NaVSp1-P has a greater steady-state open probability under depolarized conditions, and therefore, these structural differences may reflect conformational changes underlying inactivation. To further test this idea, we measured the effect of mutational perturbation at the intersubunit interface (Fig. 4) on slow inactivation. Residues lining this interface showed pronounced changes in CW spectra, lipid accessibility, and DEER distances. Compared with WT, the F170C mutant showed enhanced inactivation manifested as a greater use-dependent reduction of peak amplitude in response to a prolonged train of brief depolar-

izing pulses (at both 0.2 Hz and 1 Hz stimulations; Fig. 8 A). It is notable that NaVSp1-WT had very little inactivation in response to low-frequency stimulation at 0.2 Hz. In comparison to WT, F170C shows a small left shift in voltage-dependence of steady-state inactivation (Fig. 8 B). The mutation also results in a decrease in the time constant of inactivation; the effect is most pronounced at 10 mV (Fig. 8 C). This finding further underscores the role of the intersubunit pocket in the slow inactivation mechanism.

Discussion

Disruption of Na_v slow inactivation is associated with numerous diseases such as epilepsy, hyperkalemic periodic paralysis, myotonia, idiopathic ventricular fibrillation, and long-QT syndrome (Vilin and Ruben, 2001; Bendahhou et al., 2002; George, 2005; Andavan and Lemmens-Gruber, 2011; Dib-Hajj et al., 2013; Leipold et al., 2013). Several therapeutic drugs (local anesthetics, anticonvulsants, and antiarrhythmics), toxins (batrachotoxin, grayanotoxins, and brevetoxin), and bioactive membrane lipids (polyunsaturated fatty acids such as DHA, EPA, and ALA) modify Na_v function by targeting the slow-inactivated state (Schauf,

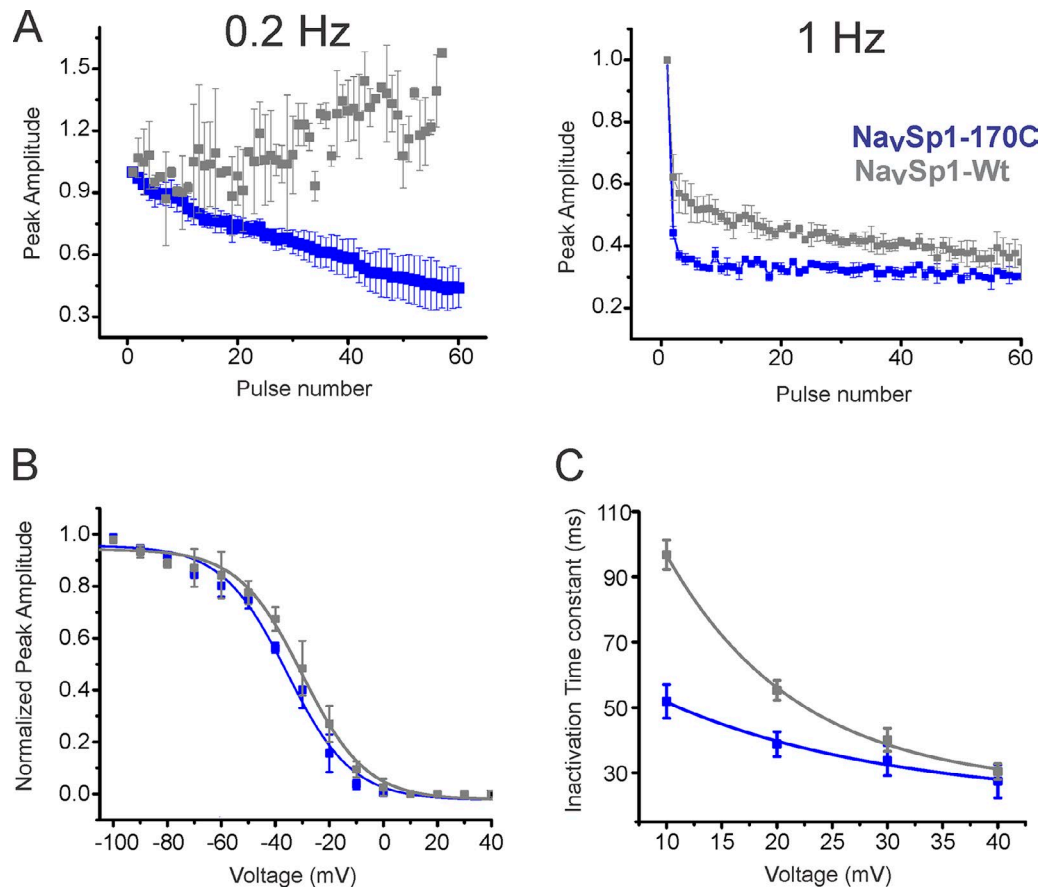


Figure 8. Electrophysiological characterization of slow inactivation in a mutant channel Na_vSp1-170C. (A) Use-dependent development of slow inactivation: depolarizations from a holding potential of -120 mV to 20 mV were applied at 0.2 Hz (left, for 200 ms in duration) and 1 Hz (right, for 150 ms in duration) frequencies, and the normalized peak current for each pulse was plotted as a function of the pulse number for Na_vSp1-WT (gray squares) and Na_vSp1-F170C (blue squares). The error bars denote SDs from $n = 4$ for Na_vSp1-WT and $n = 5$ for Na_vSp1-F170C. (B) Voltage dependence of inactivation: peak currents were measured during test pulses to 20 mV after a 2-s inactivating pulse to the indicated potentials. Values from individual experiments were normalized to the maximum test pulse currents. Inactivation curves were fit with a Boltzmann equation, $1/(1 + \exp[(V - V_h)/k_h])$, where V_h is the half-inactivation voltage and k_h is the slope factor. For Na_vSp1-WT, mean V_h was -30.3 ± 1.7 mV ($n = 4$); for Na_vSp1-F170C ($n = 4$), V_h was -35.7 ± 1.3 mV. (C) Time constants of inactivation versus voltage curves for Na_vSp1-WT (gray squares, $n = 4$) and Na_vSp1-F170C (blue squares, $n = 4$) obtained by fitting a single exponential to the current decay during depolarization to shown potentials from a holding potential of -120 mV.

1987; Balser et al., 1996b; Leifert et al., 1999; Xiao et al., 2001; Sheets et al., 2010; Song et al., 2011; Moreno et al., 2012; Kalia et al., 2015). Although the inactivation mechanisms have been studied for decades, structural insight into the Na_v slow-inactivated state is sparse, and the extent to which different regions contribute to impeding ion permeation is still unclear.

Here we probed the conformational dynamics of the SF region in membrane-reconstituted Na_v full-length and PD channels to delineate the structural changes underlying transition from the conductive to the slow-inactivated state. Spectral line shapes, as well as accessibility data, suggest that the SF region undergoes extensive conformational changes in the slow-inactivated state. Distance distributions reveal a pattern of changes that is also consistent with the slow-inactivated state being highly dynamic. For Na_vSp1, both the CW spectra, as well as distance distributions, reveal two sets of components, one that matches with Na_vSp1-P and an additional component. Multi-component distributions could arise from an ensemble of channel population belonging to conductive and slow-in-

activated states. Alternatively, asymmetric movements of individual subunits could also result in additional components. Such a loss of symmetry is in agreement with the closed pore WT-Na_vAb, Ca_vAb, and Na_vRh structures that are suggested to represent inactivated states (Payandeh et al., 2012; Zhang et al., 2012; Tang et al., 2016). However, the extent of conformational changes seen in these structures is much smaller than what is inferred from EPR data. Interestingly, in Ca_vAb structures, it appears that drug binding within the inner vestibule or along the pore causes the asymmetry (Tang et al., 2016). However, it is important to note that there are crystal structures of Na_vMs-P bound to local anesthetics that do not adopt an asymmetric conformation (Bagnéris et al., 2014), suggesting that further studies need to be done to fully understand the role of asymmetric collapse in slow inactivation.

In comparison to the conformation of the SF region in Na_vSp1-P, there is an inward motion of P1 helix toward the pore axis and an outward movement of P2 helix in Na_vSp1 (Fig. 9). If the conformation of the reconstituted Na_vSp1-P and Na_vSp1

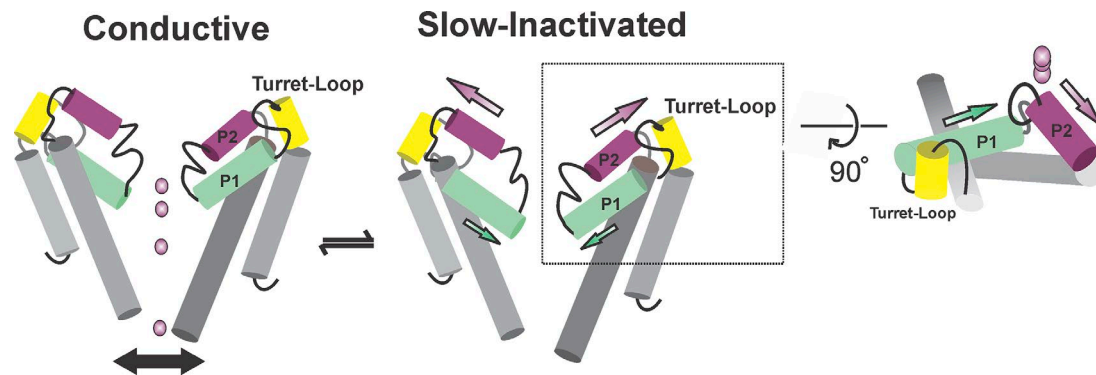


Figure 9. **An EPR-based model for the mechanism of slow inactivation at the SF region.** A cartoon representation of putative changes in the P1 and P2 helices during slow inactivation. These positional differences are likely to change intersubunit cavity volumes and hence, the accessibility of lipids and lipophilic molecules into these vestibules. The region in the inset is shown from the top (extracellular end).

were to represent the conductive and slow-inactivated states, respectively, the observed structural changes are indicative of rearrangements in the SF region that underlie slow inactivation. This rearrangement is likely to cause positional differences of the side chains at the SF, particularly the residue Glu176, which recruits Na^+ from the extracellular side and coordinates the ions within the SF. Large movements of Glu176 side chains are observed in molecular dynamic simulations, and these motions appear to be correlated to ion binding and translocation (Chakrabarti et al., 2013; Boiteux et al., 2014). Our proposed pore helix motions are consistent with multi-microsecond simulations, which reveal extensive conformational changes in the entire SF region and are hypothesized to lead to Na_v SF distortion in the slow-inactivated state (Boiteux et al., 2014). These studies also suggest that SF fluctuations are influenced by the bending motion of S6 and overall dynamics of the PD. Additional evidence also supports the dynamic nature of the selectivity filter. Particularly, even though the conformational changes at the outer pore in the crystal structures are relatively small, the β -factors in the P1 and P2 helix are substantially higher in the putative inactivated state structures, reflecting the intrinsic mobility of this region (Payandeh et al., 2012). Further, disulphide formation in the P-loop (Bénitah et al., 1999) has been shown to be sensitive toward slow inactivation kinetics of Na_v . This suggests that proximity between residues in the SF region changes during slow inactivation. The data presented here support the concept that is analogous to C-type inactivation in K^+ channels: slow inactivation is facilitated by the structural rearrangement in the P1 and P2 loop in Na_v .

Another remarkable feature of our findings is the enhanced lipid accessibility of the intersubunit cavity. Na_v structures reveal lipid tails occupying these sites, and in simulations the lipid molecules exchange freely with the bulk (Boiteux et al., 2014). This cavity (also referred to as “fenestration”; Payandeh et al., 2011) forms a conduit connecting the membrane to the central pore cavity, and is implicated to be a pathway for lipophilic drugs (such as antiepileptic agents and local anesthetics) to enter the cavity, where they block ion permeation. Our data suggest changes in polarity, as well as a potential widening of the intersubunit pocket, brought about by the relative motions of P1 and

P2 helices. This may explain why certain Na_v inhibitors bind to the slow-inactivated states with higher affinity than to the resting or open conformation (Kambouris et al., 1998). Consistently, we show that mutational perturbation of Phe170, a conserved residue lining the intersubunit cavity, has a pronounced effect on inactivation. Similar findings have been previously reported for cardiac $\text{Na}_v1.5$, where naturally occurring mutation to Ser side chain at the analogous position in domain IV significantly enhances inactivation and is associated with disease phenotype (Otagiri et al., 2008). The mutation F1705S causes a hyperpolarizing shift of steady-state inactivation and delayed recovery from inactivation, which further reduces the availability of Na_v channels and delays the conduction of cardiac impulses. Additionally, several other P1 helix mutations are reported to alter slow inactivation kinetics in multiple Na_v homologues (Vilin et al., 2001; Tan et al., 2006).

Besides the SF region, two other key domains are associated with slow inactivation: the VSD and the C-terminal end of S6. The movement of the VSD during activation has been shown to correlate with conformational changes during slow inactivation (Ruben et al., 1992; Kontis and Goldin, 1997; Capes et al., 2012; Silva and Goldstein, 2013), presumably through interaction of the VSD with the extracellular end of the PD, and thereby imparting voltage dependence to this process. Clearly, the lack of slow inactivation in the PD highlights the role of VSD in this process. Although our study does not directly probe the VSD-PD interaction, spectral changes in the turret-loop in $\text{Na}_v\text{Sp1}$ and $\text{Na}_v\text{Sp1-P}$ suggest that this region might couple the movements within the two domains. Further, the cytoplasmic regions at the C-terminal end of the S6 activation gate, referred to as the “neck” region, are also implicated in activation and slow inactivation gating (Bagn  ris et al., 2014; Arrigoni et al., 2016). EPR spectroscopic data from multiple Na_v homologues suggest that this region unwinds during channel opening (McCusker et al., 2012; Arrigoni et al., 2016).

Overall, this study provides molecular insights into protein motions associated with Na_v slow inactivation at the level of the SF region. Future studies will illuminate the mechanism of coupling between the activation gate at the S6 C-terminal end and the SF region of the channel.

Acknowledgments

We are very grateful to the members of the Chakrapani laboratory for critical reading and comments on the manuscript. The NavSp1 and NavSp1-P clones were a gift from Dr. Daniel Minor, Jr. (University of California, San Francisco, San Francisco, California)

This work was supported by an American Heart Association grant (NCRP Scientist Development Grant 12SDG12070069) and National Institutes of Health grants (R01GM108921, R01GM108921-03S1 to S. Chakrapani and 1R01HL094450 to I. Deschênes).

The authors declare no competing financial interests.

Author contributions: S. Chatterjee and S. Chakrapani conceived the project and designed experimental procedures. S. Chatterjee, S. Chalamalasetti, and R. Vyas carried out CW-EPR measurements and prepared samples for DEER measurements. I.D. Sahu collected DEER data. J. Clatot, X. Wan, and S. Chatterjee carried out patch-clamp recordings. G.A. Lorigan and I. Deschênes directed DEER data collection and electrophysiology measurements, respectively. S. Chatterjee and S. Chakrapani wrote the paper, and all authors contributed to the discussion of the paper and approved the final version.

Merritt C. Maduke served as editor.

Submitted: 2 May 2018

Accepted: 6 July 2018

References

- Ahern, C.A., J. Payandeh, F. Bosmans, and B. Chanda. 2016. The hitchhiker's guide to the voltage-gated sodium channel galaxy. *J. Gen. Physiol.* 147:1–24. <https://doi.org/10.1085/jgp.201511492>
- Altenbach, C., W. Froncisz, R. Hemker, H. McHaourab, and W.L. Hubbell. 2005. Accessibility of nitroxide side chains: absolute Heisenberg exchange rates from power saturation EPR. *Biophys. J.* 89:2103–2112. <https://doi.org/10.1529/biophysj.105.059063>
- Andavan, G.S., and R. Lemmens-Gruber. 2011. Voltage-gated sodium channels: mutations, channelopathies and targets. *Curr. Med. Chem.* 18:377–397. <https://doi.org/10.2174/092986711794839133>
- Armstrong, C.M., F. Bezanilla, and E. Rojas. 1973. Destruction of sodium conductance inactivation in squid axons perfused with pronase. *J. Gen. Physiol.* 62:375–391. <https://doi.org/10.1085/jgp.62.4.375>
- Arrigoni, C., A. Rohaim, D. Shaya, F. Findeisen, R.A. Stein, S.R. Nurva, S. Mishra, H.S. Mchaourab, and D.L. Minor Jr. 2016. Unfolding of a Temperature-Sensitive Domain Controls Voltage-Gated Channel Activation. *Cell.* 164:922–936. <https://doi.org/10.1016/j.cell.2016.02.001>
- Bagn  ris, C., P.G. DeCaen, C.E. Naylor, D.C. Pryde, I. Nobeli, D.E. Clapham, and B.A. Wallace. 2014. Prokaryotic NavMs channel as a structural and functional model for eukaryotic sodium channel antagonism. *Proc. Natl. Acad. Sci. USA.* 111:8428–8433. <https://doi.org/10.1073/pnas.1406855111>
- Balser, J.R., H.B. Nuss, N. Chiamvimonvat, M.T. P  rez-Garc  a, E. Marban, and G.F. Tomaselli. 1996a. External pore residue mediates slow inactivation in mu 1 rat skeletal muscle sodium channels. *J. Physiol.* 494:431–442. <https://doi.org/10.1113/jphysiol.1996.sp021503>
- Balser, J.R., H.B. Nuss, D.W. Orias, D.C. Johns, E. Marban, G.F. Tomaselli, and J.H. Lawrence. 1996b. Local anesthetics as effectors of allosteric gating. Lidocaine effects on inactivation-deficient rat skeletal muscle Na channels. *J. Clin. Invest.* 98:2874–2886. <https://doi.org/10.1172/JCI119116>
- Bendahhou, S., T.R. Cummins, R.W. Kula, Y.H. Fu, and L.J. Pt  cek. 2002. Impairment of slow inactivation as a common mechanism for periodic paralysis in DIIS4-S5. *Neurology.* 58:1266–1272. <https://doi.org/10.1212/WNL.58.8.1266>
- B  nitah, J.P., Z. Chen, J.R. Balser, G.F. Tomaselli, and E. Marb  n. 1999. Molecular dynamics of the sodium channel pore vary with gating: interactions between P-segment motions and inactivation. *J. Neurosci.* 19:1577–1585. <https://doi.org/10.1523/JNEUROSCI.19-05-01577.1999>
- Boiteux, C., I. Vorobyov, and T.W. Allen. 2014. Ion conduction and conformational flexibility of a bacterial voltage-gated sodium channel. *Proc. Natl. Acad. Sci. USA.* 111:3454–3459. <https://doi.org/10.1073/pnas.1320907111>
- Capes, D.L., M. Arcisio-Miranda, B.W. Jarecki, R.J. French, and B. Chanda. 2012. Gating transitions in the selectivity filter region of a sodium channel are coupled to the domain IV voltage sensor. *Proc. Natl. Acad. Sci. USA.* 109:2648–2653. <https://doi.org/10.1073/pnas.1115575109>
- Catterall, W.A. 2012. Voltage-gated sodium channels at 60: structure, function and pathophysiology. *J. Physiol.* 590:2577–2589. <https://doi.org/10.1113/jphysiol.2011.224204>
- Catterall, W.A., and T.M. Swanson. 2015. Structural Basis for Pharmacology of Voltage-Gated Sodium and Calcium Channels. *Mol. Pharmacol.* 88:141–150. <https://doi.org/10.1124/mol.114.097659>
- Chakrabarti, N., C. Ing, J. Payandeh, N. Zheng, W.A. Catterall, and R. Pom  s. 2013. Catalysis of Na⁺ permeation in the bacterial sodium channel Na(V) Ab. *Proc. Natl. Acad. Sci. USA.* 110:11331–11336. <https://doi.org/10.1073/pnas.1309452110>
- Chakrapani, S., J.F. Cordero-Morales, and E. Perozo. 2007. A quantitative description of KcsA gating I: macroscopic currents. *J. Gen. Physiol.* 130:465–478. <https://doi.org/10.1085/jgp.200709843>
- Chiang, Y.W., P.P. Borbat, and J.H. Freed. 2005. The determination of pair distance distributions by pulsed ESR using Tikhonov regularization. *J. Magn. Reson.* 172:279–295. <https://doi.org/10.1016/j.jmr.2004.10.012>
- Cortes, D.M., L.G. Cuello, and E. Perozo. 2001. Molecular architecture of full-length KcsA: role of cytoplasmic domains in ion permeation and activation gating. *J. Gen. Physiol.* 117:165–180. <https://doi.org/10.1085/jgp.117.2.165>
- Delcour, A.H., B. Martinac, J. Adler, and C. Kung. 1989. Modified reconstitution method used in patch-clamp studies of Escherichia coli ion channels. *Biophys. J.* 56:631–636. [https://doi.org/10.1016/S0006-3495\(89\)82710-9](https://doi.org/10.1016/S0006-3495(89)82710-9)
- Dib-Hajj, S.D., Y. Yang, J.A. Black, and S.G. Waxman. 2013. The Na(V)1.7 sodium channel: from molecule to man. *Nat. Rev. Neurosci.* 14:49–62. <https://doi.org/10.1038/nrn3404>
- Farahbakhsh, Z.T., C. Altenbach, and W.L. Hubbell. 1992. Spin labeled cysteines as sensors for protein-lipid interaction and conformation in rhodopsin. *Photochem. Photobiol.* 56:1019–1033. <https://doi.org/10.1111/j.1751-1097.1992.tb09725.x>
- Fozzard, H.A., P.J. Lee, and G.M. Lipkind. 2005. Mechanism of local anesthetic drug action on voltage-gated sodium channels. *Curr. Pharm. Des.* 11:2671–2686. <https://doi.org/10.2174/1381612054546833>
- George, A.L. Jr. 2005. Inherited disorders of voltage-gated sodium channels. *J. Clin. Invest.* 115:1990–1999. <https://doi.org/10.1172/JCI25505>
- Gross, A., and W.L. Hubbell. 2002. Identification of protein side chains near the membrane-aqueous interface: a site-directed spin labeling study of KcsA. *Biochemistry.* 41:1123–1128. <https://doi.org/10.1021/bi015828s>
- Hille, B. 1977. Local anesthetics: hydrophilic and hydrophobic pathways for the drug-receptor reaction. *J. Gen. Physiol.* 69:497–515. <https://doi.org/10.1085/jgp.69.4.497>
- Hille, B. 2001. Ion Channels of Excitable Membranes. Third edition. Sinauer Associates Inc., Sunderland, MA.
- Jeschke, G., A. Koch, U. Jonas, and A. Godt. 2002. Direct conversion of EPR dipolar time evolution data to distance distributions. *J. Magn. Reson.* 155:72–82. <https://doi.org/10.1006/jmre.2001.2498>
- Jeschke, G., V. Chechik, P. Ionita, A. Godt, H. Zimmermann, J. Banham, C.R. Timmel, D. Hilger, and H. Jung. 2006. DeerAnalysis2006—a comprehensive software package for analyzing pulsed ELDOR data. *Appl. Magn. Reson.* 30:473–498. <https://doi.org/10.1007/BF03166213>
- Jiang, Y., A. Lee, J. Chen, V. Ruta, M. Cadene, B.T. Chait, and R. MacKinnon. 2003. X-ray structure of a voltage-dependent K⁺ channel. *Nature.* 423:33–41. <https://doi.org/10.1038/nature01580>
- Kaczorowski, G.J., O.B. McManus, B.T. Priest, and M.L. Garcia. 2008. Ion channels as drug targets: the next GPCRs. *J. Gen. Physiol.* 131:399–405. <https://doi.org/10.1085/jgp.200709946>
- Kalia, J., M. Milescu, J. Salvatierra, J. Wagner, J.K. Klint, G.F. King, B.M. Olivera, and F. Bosmans. 2015. From foe to friend: using animal toxins to investigate ion channel function. *J. Mol. Biol.* 427:158–175. <https://doi.org/10.1016/j.jmb.2014.07.027>
- Kambouris, N.G., L.A. Hastings, S. Stepanovic, E. Marban, G.F. Tomaselli, and J.R. Balser. 1998. Mechanistic link between lidocaine block and inactivation probed by outer pore mutations in the rat micro1 skeletal muscle sodium channel. *J. Physiol.* 512:693–705. <https://doi.org/10.1111/j.1469-7793.1998.693bd.x>
- Kontis, K.J., and A.L. Goldin. 1997. Sodium channel inactivation is altered by substitution of voltage sensor positive charges. *J. Gen. Physiol.* 110:403–413. <https://doi.org/10.1085/jgp.110.4.403>

- Lee, S., S.J. Goodchild, and C.A. Ahern. 2012. Local anesthetic inhibition of a bacterial sodium channel. *J. Gen. Physiol.* 139:507–516. <https://doi.org/10.1085/jgp.201210779>
- Leifer, W.R., E.J. McMurchie, and D.A. Saint. 1999. Inhibition of cardiac sodium currents in adult rat myocytes by n-3 polyunsaturated fatty acids. *J. Physiol.* 520:671–679. <https://doi.org/10.1111/j.1469-7793.1999.00671.x>
- Leipold, E., L. Liebmann, G.C. Korenke, T. Heinrich, S. Giesselmann, J. Baets, M. Ebbinghaus, R.O. Goral, T. Stöckberg, J.C. Hennings, et al. 2013. A de novo gain-of-function mutation in SCN1A causes loss of pain perception. *Nat. Genet.* 45:1399–1404. <https://doi.org/10.1038/ng.2767>
- Lenaus, M.J., T.M. Gamal El-Din, C. Ing, K. Ramanadane, R. Pomès, N. Zheng, and W.A. Catterall. 2017. Structures of closed and open states of a voltage-gated sodium channel. *Proc. Natl. Acad. Sci. USA.* 114:E3051–E3060. <https://doi.org/10.1073/pnas.1700761114>
- Li, Q., S. Wanderling, P. Somporpisut, and E. Perozo. 2014. Structural basis of lipid-driven conformational transitions in the KvAP voltage-sensing domain. *Nat. Struct. Mol. Biol.* 21:160–166. <https://doi.org/10.1038/nsmb.2747>
- Long, S.B., E.B. Campbell, and R. Mackinnon. 2005. Crystal structure of a mammalian voltage-dependent Shaker family K⁺ channel. *Science.* 309:897–903. <https://doi.org/10.1126/science.1116269>
- Long, S.B., X. Tao, E.B. Campbell, and R. MacKinnon. 2007. Atomic structure of a voltage-dependent K⁺ channel in a lipid membrane-like environment. *Nature.* 450:376–382. <https://doi.org/10.1038/nature06265>
- McCusker, E.C., C. Bagnéris, C.E. Naylor, A.R. Cole, N. D'Avanzo, C.G. Nichols, and B.A. Wallace. 2012. Structure of a bacterial voltage-gated sodium channel pore reveals mechanisms of opening and closing. *Nat. Commun.* 3:1102. <https://doi.org/10.1038/ncomms2077>
- Mchaourab, H.S., M.A. Lietzow, K. Hideg, and W.L. Hubbell. 1996. Motion of spin-labeled side chains in T4 lysozyme. Correlation with protein structure and dynamics. *Biochemistry.* 35:7692–7704. <https://doi.org/10.1021/bi960482k>
- Moreno, C., A. Macías, A. Prieto, A. de la Cruz, T. González, and C. Valenzuela. 2012. Effects of n-3 Polyunsaturated Fatty Acids on Cardiac Ion Channels. *Front. Physiol.* 3:245. <https://doi.org/10.3389/fphys.2012.00245>
- Narashashi, T. 1964. Restoration of Action Potential by Anodal Polarization in Lobster Giant Axons. *J. Cell. Comp. Physiol.* 64:73–96. <https://doi.org/10.1002/jcp.1030640108>
- Nardi, A., N. Damann, T. Hertrampf, and A. Kless. 2012. Advances in targeting voltage-gated sodium channels with small molecules. *ChemMedChem.* 7:1712–1740. <https://doi.org/10.1002/cmdc.201200298>
- Nau, C., and G.K. Wang. 2004. Interactions of local anesthetics with voltage-gated Na⁺ channels. *J. Membr. Biol.* 201:1–8. <https://doi.org/10.1007/s00232-004-0702-y>
- Naylor, C.E., C. Bagnéris, P.G. DeCaen, A. Sula, A. Scaglione, D.E. Clapham, and B.A. Wallace. 2016. Molecular basis of ion permeability in a voltage-gated sodium channel. *EMBO J.* 35:820–830. <https://doi.org/10.15252/embj.201593285>
- Oelstrom, K., and B. Chanda. 2016. Congruent pattern of accessibility identifies minimal pore gate in a non-symmetric voltage-gated sodium channel. *Nat. Commun.* 7:11608. <https://doi.org/10.1038/ncomms11608>
- Otagiri, T., K. Kijima, M. Osawa, K. Ishii, N. Makita, R. Matoba, K. Umetsu, and K. Hayasaka. 2008. Cardiac ion channel gene mutations in sudden infant death syndrome. *Pediatr. Res.* 64:482–487. <https://doi.org/10.1203/PDR.0b013e3181841eca>
- Pannier, M., S. Veit, A. Godt, G. Jeschke, and H.W. Spiess. 2000. Dead-time free measurement of dipole-dipole interactions between electron spins. *J. Magn. Reson.* 142:331–340. <https://doi.org/10.1006/jmre.1999.1944>
- Pavlov, E., C. Bladen, R. Winkfein, C. Diao, P. Dhaliwal, and R.J. French. 2005. The pore, not cytoplasmic domains, underlies inactivation in a prokaryotic sodium channel. *Biophys. J.* 89:232–242. <https://doi.org/10.1529/biophysj.104.056994>
- Payandeh, J., T. Scheuer, N. Zheng, and W.A. Catterall. 2011. The crystal structure of a voltage-gated sodium channel. *Nature.* 475:353–358. <https://doi.org/10.1038/nature10238>
- Payandeh, J., T.M. Gamal El-Din, T. Scheuer, N. Zheng, and W.A. Catterall. 2012. Crystal structure of a voltage-gated sodium channel in two potentially inactivated states. *Nature.* 486:135–139. <https://doi.org/10.1038/nature11077>
- Polyhach, Y., A. Godt, C. Bauer, and G. Jeschke. 2007. Spin pair geometry revealed by high-field DEER in the presence of conformational distributions. *J. Magn. Reson.* 185:118–129. <https://doi.org/10.1016/j.jmr.2006.11.012>
- Polyhach, Y., E. Bordignon, and G. Jeschke. 2011. Rotamer libraries of spin labelled cysteines for protein studies. *Phys. Chem. Chem. Phys.* 13:2356–2366. <https://doi.org/10.1039/C0CP01865A>
- Ragsdale, D.S., J.C. McPhee, T. Scheuer, and W.A. Catterall. 1994. Molecular determinants of state-dependent block of Na⁺ channels by local anesthetics. *Science.* 265:1724–1728. <https://doi.org/10.1126/science.8085162>
- Ren, D., B. Navarro, H. Xu, L. Yue, Q. Shi, and D.E. Clapham. 2001. A prokaryotic voltage-gated sodium channel. *Science.* 294:2372–2375. <https://doi.org/10.1126/science.1065635>
- Rojas, E., and B. Rudy. 1976. Destruction of the sodium conductance inactivation by a specific protease in perfused nerve fibres from Loligo. *J. Physiol.* 262:501–531. <https://doi.org/10.1113/jphysiol.1976.sp011608>
- Ruben, P.C., J.G. Starkus, and M.D. Rayner. 1992. Steady-state availability of sodium channels. Interactions between activation and slow inactivation. *Biophys. J.* 61:941–955. [https://doi.org/10.1016/S0006-3495\(92\)81901-X](https://doi.org/10.1016/S0006-3495(92)81901-X)
- Rudy, B. 1978. Slow inactivation of the sodium conductance in squid giant axons. Pronase resistance. *J. Physiol.* 283:1–21. <https://doi.org/10.1113/jphysiol.1978.sp012485>
- Sandtner, W., J. Szendroedi, T. Zarrabi, E. Zebadin, K. Hilber, I. Glaaser, H.A. Fozzard, S.C. Dudley, and H. Todt. 2004. Lidocaine: a foot in the door of the inner vestibule prevents ultra-slow inactivation of a voltage-gated sodium channel. *Mol. Pharmacol.* 66:648–657.
- Schauf, C.L. 1987. Zonisamide enhances slow sodium inactivation in Myxicola. *Brain Res.* 413:185–188. [https://doi.org/10.1016/0006-8993\(87\)90168-5](https://doi.org/10.1016/0006-8993(87)90168-5)
- Schmidt, D., Q.X. Jiang, and R. MacKinnon. 2006. Phospholipids and the origin of cationic gating charges in voltage sensors. *Nature.* 444:775–779. <https://doi.org/10.1038/nature05416>
- Shaya, D., M. Kreir, R.A. Robbins, S. Wong, J. Hammon, A. Brüggemann, and D.L. Minor Jr. 2011. Voltage-gated sodium channel (Na_v) protein dissection creates a set of functional pore-only proteins. *Proc. Natl. Acad. Sci. USA.* 108:12313–12318. <https://doi.org/10.1073/pnas.1106811108>
- Shaya, D., F. Findeisen, F. Abderemane-Ali, C. Arrigoni, S. Wong, S.R. Nurva, G. Loussouarn, and D.L. Minor Jr. 2014. Structure of a prokaryotic sodium channel pore reveals essential gating elements and an outer ion binding site common to eukaryotic channels. *J. Mol. Biol.* 426:467–483. <https://doi.org/10.1016/j.jmb.2013.10.010>
- Sheets, M.F., H.A. Fozzard, G.M. Lipkind, and D.A. Hanck. 2010. Sodium channel molecular conformations and antiarrhythmic drug affinity. *Trends Cardiovasc. Med.* 20:16–21. <https://doi.org/10.1016/j.tcm.2010.03.002>
- Silva, J. 2014. Slow inactivation of Na⁺ channels. *Handb. Exp. Pharmacol.* 221:33–49. https://doi.org/10.1007/978-3-642-41588-3_3
- Silva, J.R., and S.A. Goldstein. 2013. Voltage-sensor movements describe slow inactivation of voltage-gated sodium channels I: wild-type skeletal muscle Na_v1.4. *J. Gen. Physiol.* 141:309–321. <https://doi.org/10.1085/jgp.201210909>
- Song, W., K.S. Silver, Y. Du, Z. Liu, and K. Dong. 2011. Analysis of the action of lidocaine on insect sodium channels. *Insect Biochem. Mol. Biol.* 41:36–41. <https://doi.org/10.1016/j.ibmb.2010.09.010>
- Sula, A., J. Booker, L.C. Ng, C.E. Naylor, P.G. DeCaen, and B.A. Wallace. 2017. The complete structure of an activated open sodium channel. *Nat. Commun.* 8:14205. <https://doi.org/10.1038/ncomms14205>
- Szendroedi, J., W. Sandtner, T. Zarrabi, E. Zebadin, K. Hilber, S.C. Dudley Jr., H.A. Fozzard, and H. Todt. 2007. Speeding the recovery from ultraslow inactivation of voltage-gated Na⁺ channels by metal ion binding to the selectivity filter: a foot-on-the-door? *Biophys. J.* 93:4209–4224. <https://doi.org/10.1529/biophysj.107.104794>
- Tan, B.H., C.R. Valdivia, C. Song, and J.C. Makielski. 2006. Partial expression defect for the SCN5A missense mutation G1406R depends on splice variant background Q1077 and rescue by mexiletine. *Am. J. Physiol. Heart Circ. Physiol.* 291:H1822–H1828. <https://doi.org/10.1152/ajpheart.00101.2006>
- Tang, L., T.M. Gamal El-Din, T.M. Swanson, D.C. Pryde, T. Scheuer, N. Zheng, and W.A. Catterall. 2016. Structural basis for inhibition of a voltage-gated Ca²⁺ channel by Ca²⁺ antagonist drugs. *Nature.* 537:117–121. <https://doi.org/10.1038/nature19102>
- Toib, A., V. Lyakhov, and S. Marom. 1998. Interaction between duration of activity and time course of recovery from slow inactivation in mammalian brain Na⁺ channels. *J. Neurosci.* 18:1893–1903. <https://doi.org/10.1523/JNEUROSCI.18-05-01893.1998>
- Townsend, C., and R. Horn. 1997. Effect of alkali metal cations on slow inactivation of cardiac Na⁺ channels. *J. Gen. Physiol.* 110:23–33. <https://doi.org/10.1085/jgp.110.1.23>
- Ulbricht, W. 2005. Sodium channel inactivation: molecular determinants and modulation. *Physiol. Rev.* 85:1271–1301. <https://doi.org/10.1152/physrev.00024.2004>

- Velisetty, P., and S. Chakrapani. 2012. Desensitization mechanism in prokaryotic ligand-gated ion channel. *J. Biol. Chem.* 287:18467–18477. <https://doi.org/10.1074/jbc.M112.348045>
- Velisetty, P., S.V. Chalamalasetti, and S. Chakrapani. 2012. Conformational transitions underlying pore opening and desensitization in membrane-embedded *Gloeobacter violaceus* ligand-gated ion channel (GLIC). *J. Biol. Chem.* 287:36864–36872. <https://doi.org/10.1074/jbc.M112.401067>
- Vilin, Y.Y., and P.C. Ruben. 2001. Slow inactivation in voltage-gated sodium channels: molecular substrates and contributions to channelopathies. *Cell Biochem. Biophys.* 35:171–190. <https://doi.org/10.1385/CBB:35:2:171>
- Vilin, Y.Y., E. Fujimoto, and P.C. Ruben. 2001. A single residue differentiates between human cardiac and skeletal muscle Na⁺ channel slow inactivation. *Biophys. J.* 80:2221–2230. [https://doi.org/10.1016/S0006-3495\(01\)76195-4](https://doi.org/10.1016/S0006-3495(01)76195-4)
- von Hagens, T., Y. Polyhach, M. Sajid, A. Godt, and G. Jeschke. 2013. Suppression of ghost distances in multiple-spin double electron-electron resonance. *Phys. Chem. Chem. Phys.* 15:5854–5866. <https://doi.org/10.1039/c3cp44462g>
- Xiao, Y.F., Q. Ke, S.Y. Wang, K. Auktor, Y. Yang, G.K. Wang, J.P. Morgan, and A. Leaf. 2001. Single point mutations affect fatty acid block of human myocardial sodium channel alpha subunit Na⁺ channels. *Proc. Natl. Acad. Sci. USA.* 98:3606–3611. <https://doi.org/10.1073/pnas.061003798>
- Zhang, X., W. Ren, P. DeCaen, C. Yan, X. Tao, L. Tang, J. Wang, K. Hasegawa, T. Kumasaka, J. He, et al. 2012. Crystal structure of an orthologue of the NaChBac voltage-gated sodium channel. *Nature.* 486:130–134. <https://doi.org/10.1038/nature11054>
- Zheng, H., W. Liu, L.Y. Anderson, and Q.X. Jiang. 2011. Lipid-dependent gating of a voltage-gated potassium channel. *Nat. Commun.* 2:250. <https://doi.org/10.1038/ncomms1254>
- Zou, P., and H.S. McHaourab. 2010. Increased sensitivity and extended range of distance measurements in spin-labeled membrane proteins: Q-band double electron-electron resonance and nanoscale bilayers. *Biophys. J.* 98:L18–L20. <https://doi.org/10.1016/j.bpj.2009.12.4193>